Chinese Chemical Letters 36 (2025) 110136

Contents lists available at ScienceDirect

Chinese Chemical Letters

journal homepage: www.elsevier.com/locate/cclet

Hierarchical Fe-Bi/$Bi_7O_9I_3$/OVs microspheres coupled with natural air diffusion electrode to achieve efficient heterogeneous visible-light-driven photoelectro-Fenton degradation of tetracycline without aeration

Ruiheng Liang[a,b], Huizhong Wu[a,b], Zhongzheng Hu[a,b], Ge Song[a,b], Xuyang Zhang[a,b], Omotayo A. Arotiba[c,d], Minghua Zhou[a,b,*]

[a] Tianjin Key Laboratory of Environmental Technology for Complex Trans-Media Pollution, College of Environmental Science and Engineering, Nankai University, Tianjin 300350, China
[b] Tianjin Advanced Water Treatment Technology International Joint Research Center, College of Environmental Science and Engineering, Nankai University, Tianjin 300350, China
[c] Department of Chemical Sciences, University of Johannesburg, Doornfontein 2028, South Africa
[d] Centre for Nanomaterials Science Research, University of Johannesburg, Doornfontein 2028, South Africa

ARTICLE INFO

Article history:
Received 18 September 2023
Revised 6 June 2024
Accepted 17 June 2024
Available online 18 June 2024

Keywords:
$Bi_7O_9I_3$
Fe doping
Heterogeneous visible-light-driven photoelectron-Fenton
Plasmonic Bi
Oxygen vacancies

ABSTRACT

A novel Fe-doping three-dimensional flower-like $Bi_7O_9I_3$ microspheres with plasmonic Bi and rich surface oxygen vacancies (Fe-Bi/$Bi_7O_9I_3$/OVs) was prepared as catalysts, and further coupled with natural air diffusion electrode (NADE) to construct the heterogeneous visible-light-driven photoelectro-Fenton (HE-VL-PEF) process to enhance the degradation and mineralization of tetracycline (TC). Interfacial ≡Fe sites, OVs and Bi metal were simultaneously constructed *via* Fe doping, which effectively improved visible light absorption and the separation efficiency of photogenerated carriers to further accelerate the transformation of Fe(III) to Fe(II), achieving Fenton reaction recycling. HE-VL-PEF process could achieve enhanced treatment of pollutants, thanks to the synergistic effect of electro-Fenton (EF) and photo-Fenton (PF). NADE exhibited excellent H_2O_2 electrosynthesis without external oxygen-pumping equipment. Under the irradiation of visible light, Fe-Bi/$Bi_7O_9I_3$/OVs could achieve more photoelectrons to accelerate the transformation of Fe(III) to Fe(II) or directly activate H_2O_2. DFT calculations also clearly demonstrated that except for the fast charge separation and transfer, Fe-Bi/$Bi_7O_9I_3$/OVs could achieve a faster electron transport between Fe-O, facilitating Fe site acquire more electron. Consequently, the Fe-Bi/$Bi_7O_9I_3$/OVs in HE-VL-PEF process presented performance superiorities including excellent pollutant removal (91.91%), low electric energy consumption of 66.34 kWh/kg total organic carbon (TOC), excellent reusability and wide pH adaptability (3–9).

Nowadays antibiotics has been widely and commonly used in clinical medicine, animal husbandry and agriculture for their excellent performance to treat bacterial infections [1,2]. However, the abuse and emission of antibiotics possesses huge threats to the ecosystems and human health [3]. Particularly, tetracycline (TC), as one of the most common antibiotics all over the world, has high ecotoxicity, environmental durability and been frequently detected in the surface and ground water [4,5]. Due to its chemical stability and solubility in water, TC cannot be easily degraded through biological processes and conventional wastewater treatments [6,7]. Therefore, it is indispensable to develop a highly efficient technology to remove TC from wastewater.

Advanced oxidation processes (AOPs) based on generating highly reactive radical species have been considered as an efficient technology to degrade and mineralize refractory contaminants [8,9]. Among many AOPs, Fenton process can generate strongly oxidizing hydroxyl radicals (•OH) *via* the decomposition of hydrogen peroxide (H_2O_2) by ferrous ions (Fe(II)) in aqueous solution, which has been currently widely used in pharmaceuticals wastewater treatment [10,11]. However, the continuous production of •OH by conventional Fenton reaction is largely restricted by the sluggish regeneration of Fe(II) and the need for continu-

* Corresponding author.
E-mail address: zhoumh@nankai.edu.cn (M. Zhou).

https://doi.org/10.1016/j.cclet.2024.110136
1001-8417/

ous addition of H_2O_2, which greatly increases the operating costs [12,13].

Aim to overcome the drawback of conventional Fenton process, electro-Fenton (EF) process and photo-Fenton (PF) have been proposed [14]. EF can achieve the *in-situ* electro-generation of H_2O_2 *via* the cathodic two-electron oxygen reduction reaction (ORR), which avoids the storage and transportation of H_2O_2 [15]. But, as occurs in conventional Fenton process, the transformation rate of Fe(III) to Fe(II) is the crucial rate-limiting step of the EF [13]. Notable, the transformation efficiency of Fe(III) to Fe(II) can be improved *via* the photogenerated electron derived from photocatalysis to accelerate Fenton reaction [16]. Hence, the photo-Fenton process has attracted great interest in wastewater treatment. However, it still needs to be additionally added H_2O_2 like conventional Fenton process. As a result, it is important to construct a Fenton-based process with strong ability to supply electrons and H_2O_2.

Heterogeneous photoelectro-Fenton (HE-PEF) process combines the benefits of EF and PF process, achieves the *in-situ* electro-generation of H_2O_2 and accelerate the transformation of Fe(III) to Fe(II) by photogenerated electron, successfully improving the efficiency of the degradation and mineralization of organic micropollutants. Furthermore, H_2O_2 as photogenerated electron acceptor also promote the separation of photogenerated charge carriers (e^-/h^+) and generate more reactive oxygen species (ROS) [17]. Compared with traditional light sources such as mercury or xenon lamps, light emitting diode (LED) has more environmentally friendly characteristics such as lower energy consumption, longer service life, less toxicity, and smaller occupation space. As a result, PEF process, especially being driven by LED visible light irradiation, has attracted considerable attentions.

However, the catalytic performance of most of HE-PEF catalysts has remained limited due to the fast recombination rate of photogenerated electron–hole, the poor chemical stability and insufficient optical absorption in the visible region [18]. As one of bismuth halide oxide ($Bi_xO_yX_z$), $Bi_7O_9I_3$ has displayed excellent photocatalytic activity since its excellent layered structure [19]. To activate H_2O_2 more efficiently, the introduction of reaction site for constructing Fenton reaction in the presence of H_2O_2 is crucial [20,21]. Meanwhile, the existence of oxygen vacancies can promote the transfer of photogenerated electrons and accelerate the redox cycling of ≡Fe(III)/≡Fe(II) to boost the activation of H_2O_2 for generating more $^{\bullet}OH$ [19,20]. Furthermore, the existence of surface plasmon resonance (SPR) absorption from Bi metal enables the photocatalyst to achieve full spectral response, especially enhanced absorption in the visible light range [22].

Furthermore, as one of H_2O_2-based electrochemical advanced oxidation processes (EAOPs), cathode materials that can efficiently produce H_2O_2 are crucial for HE-VL-PEF process. The most commonly used cathode materials are gas diffusion electrodes (GDE) and graphite felt (GF) due to their high H_2O_2 production efficiency and low cost [23]. However, both GDE and GF require aeration to supply sufficient O_2 for ORR and have extremely low oxygen utilization efficiency (OUE) (usually $<1\%$), which results in the high aeration energy consumption (0.04–0.5 kWh/m^3) [24]. In our previous research, a natural air diffusion electrode (NADE) with a superhydrophobic three-phase interface has achieved better H_2O_2 electrosynthesis performance without external oxygen-pumping equipment, showing great application potential in H_2O_2-based EAOPs [24,25].

Herein in this work, a novel three-dimensional flower-like Fe-Bi/$Bi_7O_9I_3$/OVs microspheres photocatalyst was prepared for efficiently activating H_2O_2 and coupled with NADE, accomplishing efficient heterogeneous visible light photoelectro-Fenton (HE-VL-PEF) degradation and mineralization of TC without aeration. For catalyst, interfacial ≡Fe sites, OVs and Bi metal were simultaneously constructed in hierarchical $Bi_7O_9I_3$ microspheres *via* a facile Fe doping, which introduced Fenton reaction site (≡Fe), broadened the light response range and improved the separation efficiency of photogenerated carriers to further accelerate the transformation of Fe(III) to Fe(II), achieving Fenton reaction recycling. HE-VL-PEF process could achieve the synergistic of EF and PF under LED visible light irradiation for enhanced treatment effect on pollutants.

The crystalline structures of as-prepared catalysts were confirmed through the X-ray diffraction (XRD) technique. Fig. 1a showed XRD patterns of the $Bi_7O_9I_3$ and Fe-Bi/$Bi_7O_9I_3$/OVs samples. It was obvious that all diffraction peaks could be indexed to the typical tetragonal structure of BiOI (JCPDS No. 73–2062), but some peaks shifted slightly to smaller diffraction angles, which might be attributed to the existence of extra bismuth and oxygen atoms in the lattice of BiOI, resulting in the lattice distortion of the crystal structure [19,26]. Notably, it could be seen that the rhombohedral phase of Bi (JCPDS No. 44–1246) was formed in the diffraction peaks of Fe-Bi/$Bi_7O_9I_3$/OVs (Fig. S1 in Supporting information), which could be explained that thermal reduction of ethylene glycol (EG) allowed *in situ* formation of Bi^0 on the $Bi_7O_9I_3$, and Fe^{3+} contributed to the transformation of amorphous to crystalline phase (Bi^{3+} to Bi^0) [27]. Furthermore, there was no obvious peaks of Fe oxides in the XRD pattern of Fe-Bi/$Bi_7O_9I_3$/OVs, indicating that Fe existed in the form of ion doping rather than new substances [20].

The X-ray photoelectron spectra (XPS) was conducted to analyze the elemental compositions and chemical valance states of as-prepared catalysts. As shown in Fig. 1b, the XPS spectra revealed that Bi, O, and I appeared in both $Bi_7O_9I_3$ and Fe-Bi/$Bi_7O_9I_3$/OVs. Notably, Fe-Bi/$Bi_7O_9I_3$/OVs contained Fe element in addition to Bi, I and O elements. As seen from the Fe 2p spectrum (Fig. 1c), compared with $Bi_7O_9I_3$, the Fe 2p spectra of Fe-Bi/$Bi_7O_9I_3$/OVs exhibited two characteristic peaks at 710.4 eV and 723.9 eV, corresponding to the Fe $2p_{3/2}$ and Fe $2p_{1/2}$ orbitals, respectively, which can be attributed to Fe doping [19,28]. The corresponding high-resolution XPS spectra of Bi, O and I were demonstrated in Figs. 1d and e and Fig. S2 (Supporting information). As displayed in Fig. 1d, two main peaks located at 158.7 eV and 164.0 eV were observed in Fe-Bi/$Bi_7O_9I_3$/OVs, which could be assigned to Bi $4f_{7/2}$ and Bi $4f_{5/2}$ respectively [26]. Compared with $Bi_7O_9I_3$, the Bi 4f peaks of Fe-Bi/$Bi_7O_9I_3$/OVs shifted to a lower binding energy, which could be attributed to that with the higher electronegativity, Fe(III) has a stronger ability of attracting electrons than Bi^{3+}, resulting in a decrease in binding energy of Bi in the composite [20]. Furthermore, Fe(III) has a smaller ionic radius than Bi^{3+}, making it easier for Fe(III) ions to occupy Bi^{3+} sites [20]. As for I 3d spectra (Fig. S2), two main peaks located at 618.7 eV (I $3d_{5/2}$) and 630.25 eV (I $3d_{3/2}$) were observed in Fe-Bi/$Bi_7O_9I_3$/OVs. And compared with $Bi_7O_9I_3$, the I 3d peaks of Fe-Bi/$Bi_7O_9I_3$/OVs also shifted to a lower binding energy, just like the Bi 4f spectra. As displayed in Fig. 1e, the O 1s spectra could be split into three characteristic peaks. For Fe-Bi/$Bi_7O_9I_3$/OVs, the peak at 529.5 eV, 531.0 eV and 532.6 eV could be attributed to lattice oxygen of Bi-O bond, the defect oxygen at the vacancy sites and adsorbed oxygen of hydroxyl groups, respectively [29]. Compared with $Bi_7O_9I_3$, the binding energy peak area of oxygen vacancies in the Fe-Bi/$Bi_7O_9I_3$/OVs was increased, which further indicated that the Fe doping promoted the formation of more oxygen vacancies and the formation of Bi^0 would accompany the production of OVs [30].

In order to further prove the existence of more oxygen vacancies, the electron paramagnetic resonance (EPR) spectra were conducted to analyze oxygen vacancies. As shown in Fig. 1f, the signal intensity of oxygen vacancy was enhanced after Fe doping because the replacement of Fe(III) for Bi^{3+} caused partial distortion of the $Bi_7O_9I_3$ crystal structure to generate more oxygen vacancies, and the formation of Bi^0 would accompany the production of OVs [30,31]. Oxygen vacancies in Fe-Bi/$Bi_7O_9I_3$/OVs could act as the trapping center of photogenerated electrons, thus reducing

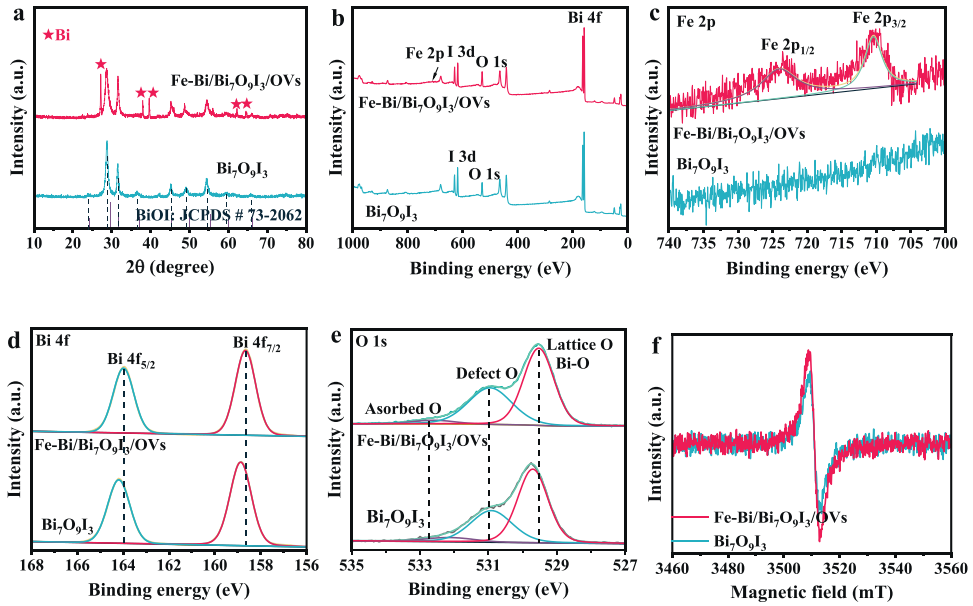

Fig. 1. (a) XRD pattern and (b) XPS spectra of $Bi_7O_9I_3$ and Fe-Bi/$Bi_7O_9I_3$/OVs. (c) The difference XPS spectra of Fe 2p, (d) Bi 4f, and (e) O 1s of $Bi_7O_9I_3$ and Fe-Bi/$Bi_7O_9I_3$/OVs. (f) EPR spectra of $Bi_7O_9I_3$ and Fe-Bi/$Bi_7O_9I_3$/OVs.

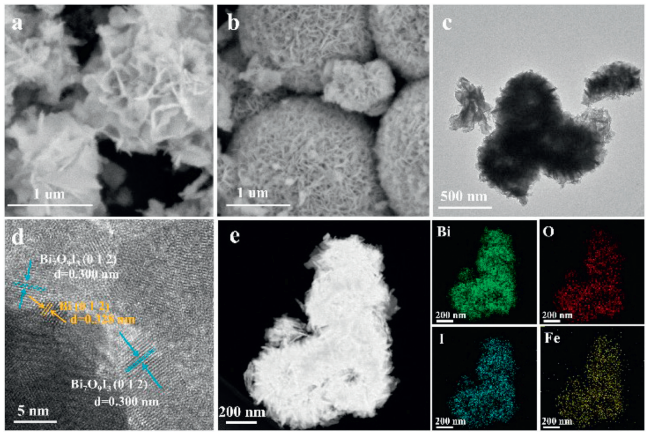

Fig. 2. (a) Field-emission scanning electron microscopy (FESEM) image of $Bi_7O_9I_3$ and (b) Fe-Bi/$Bi_7O_9I_3$/OVs. (c)TEM image, (d) HR-TEM image and (e) high-angle annular dark-field scanning transmission electron microscopy (HAADF-STEM) image and corresponding element mapping of Bi, O, I and Fe of Fe-Bi/$Bi_7O_9I_3$/OVs.

the probability of their recombination with photogenerated holes [32].

The microstructures of prepared catalysts were characterized by scanning electron microscopy (SEM), transmission electron microscopy (TEM) and high-resoultion TEM (HRTEM). As shown in Fig. 2a, $Bi_7O_9I_3$ appeared as flower-like hierarchical architectures. Fe-Bi/$Bi_7O_9I_3$/OVs also shows flower-like microspheres with a radius of 1 um (Fig. 2b). After Fe doping, the self-assembled nanosheets aggregated, showing the morphology of microspheres. TEM images further confirmed the hierarchical flower-like microspheres architecture of Fe-Bi/$Bi_7O_9I_3$/OVs (Fig. 2c). Meanwhile, as displayed in Fig. 2d, the lattice fringes with 0.300 nm and 0.328 nm lattice spacing are attributed to (012) crystal plane of $Bi_7O_9I_3$ and (012) lattice plane of Bi, respectively. Furthermore, according to corresponding element mapping results (Fig. 2e), all elements (Bi, O, I and Fe) could be clearly observed, indicating that Fe ions had been homogeneously doped into the $Bi_7O_9I_3$ crystal structure, which was consistent with XPS results.

The transient photocurrent responses were carried out to analyze the photogenerated charge separation of the photocatalysts. As shown in Fig. 3a, the Fe-Bi/$Bi_7O_9I_3$/OVs (20.85 μA/cm^2) exhibited higher photocurrent intensity under visible light irradiation compared with $Bi_7O_9I_3$ (12.75 μA/cm^2), revealing the superior charge separation dynamics, suggesting that the existence of plasmatic Bi and oxygen vacancies accelerated the transfer of photogenerated e^- and h^+ [32]. Compared with $Bi_7O_9I_3$, Fe-Bi/$Bi_7O_9I_3$/OVs showed much steeper and larger photocurrent density (Fig. 3b), which also indicated that it possessed superior charge separation dynamics. The EIS Nyquist curves of Fe-Bi/$Bi_7O_9I_3$/OVs and $Bi_7O_9I_3$ were shown in Fig. 3c, it is obvious that Fe-Bi/$Bi_7O_9I_3$/OVs possessed smaller semicircle radius compared with pristine $Bi_7O_9I_3$, indicating a faster charge transfer kinetics at Fe-Bi/$Bi_7O_9I_3$/OVs electrolyte interface effective inhibited photogenerated charge recombination. The semicircle radius on the EIS Nyquist curves of Fe-Bi/$Bi_7O_9I_3$/OVs measured without visible light irradiation decreased obviously (Fig. S3 in Supporting information), implying a large of number of photogenerated charge generated under illumination [33]. The separation of e^- and h^+ in different catalysts were demonstrated by combining the analysis of photoluminescence spectra (PL). Compared with pure $Bi_7O_9I_3$, the Fe-Bi/$Bi_7O_9I_3$/OVs exhibited weaker intensity due to the enhanced photogenerated carriers separation efficiency (Fig. S4 in Supporting information), which was consistent well with the photocurrent analysis and EIS analysis. The enhanced photocurrent and less resistance indicated effective transport of photogenerated carriers over Fe-Bi/$Bi_7O_9I_3$/OVs, which could be ascribed to the existence of plasmatic Bi and oxygen vacancies induced by Fe-doping.

The UV–vis adsorption spectra of Fe-Bi/$Bi_7O_9I_3$/OVs and $Bi_7O_9I_3$ were displayed in Fig. 3d. The absorption edges of $Bi_7O_9I_3$ and Fe-Bi/$Bi_7O_9I_3$/OVs were 553 nm and 663 nm, respectively. Compared with $Bi_7O_9I_3$, the absorption edges of Fe-Bi/$Bi_7O_9I_3$/OVs witnessed an obvious redshift. The existence of plasmatic Bi (SPR effect) and oxygen vacancies significantly broaden the range of photoresponse, resulting in an enhancement of the utilization of visible light [34,35]. The bandgap of $Bi_7O_9I_3$ and Fe-Bi/$Bi_7O_9I_3$ could be calculated using Eq. 1.

$$\alpha h\nu = A\left(h\nu - E_g\right)^{n/2} \quad (1)$$

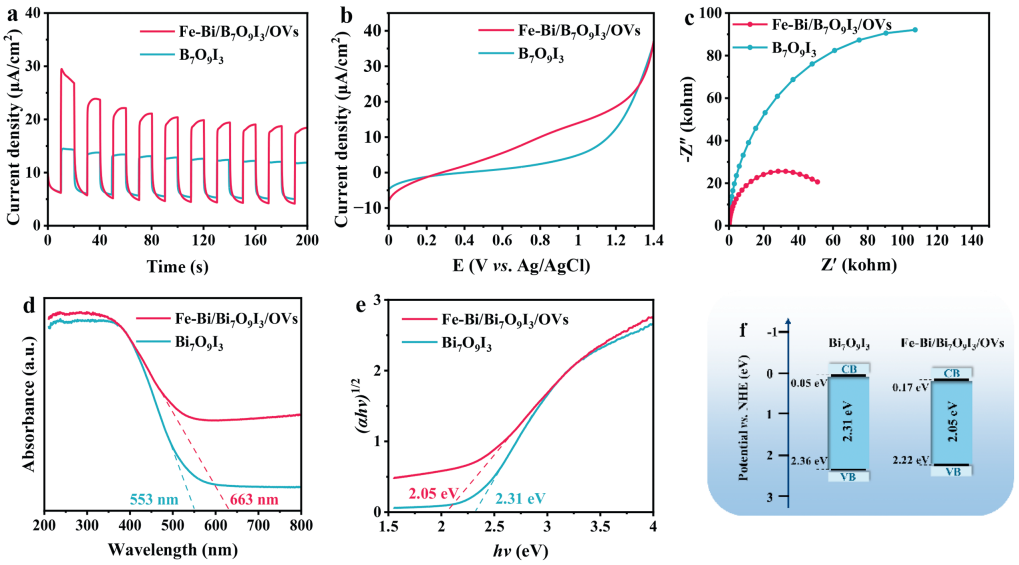

Fig. 3. (a) Transient photocurrent response under the light on/off conditions. (b) The linear sweep voltammetry under visible light irradiation. (c) EIS Nyquist plots under visible light irradiation. (d) UV–vis absorbance spectra, (e) Tauc plots and (f) energy band structures of Fe-Bi/$Bi_7O_9I_3$/OVs and $Bi_7O_9I_3$.

where α represents absorption coefficient, A represents proportional constant, h represents Planck constant, v represents light frequency, E_g represents bandgap energy and n is 4 for indirect band gap semiconductor [36]. The calculated E_g of $Bi_7O_9I_3$ and Fe-Bi/$Bi_7O_9I_3$/OVs were 2.31 eV and 2.05 eV, respectively (Fig. 3e). As shown in Fig. S5 (Supporting information), it is obvious that the slope of the Mott-Schottky plots was positive, indicating that both $Bi_7O_9I_3$ and Fe-Bi/$Bi_7O_9I_3$/OVs were n-type semiconductors [37]. The flat band potential of $Bi_7O_9I_3$ and Fe-Bi/$Bi_7O_9I_3$/OVs approximately were −0.28 and −0.16 eV (*vs.* Ag/AgCl), corresponding to 0.15 and 0.27 eV (*vs.* NHE), respectively. Since the conduction band position of the n-type semiconductor is usually negative approximated 0.1–0.2 V than the flat-band position [38]. Herein, the conduction band potential (E_{CB}) of $Bi_7O_9I_3$ and Fe-Bi/$Bi_7O_9I_3$/OVs were 0.05 and 0.17 eV (*vs.* NHE) when 0.1 eV was taken. Combined with the bandgap, the valence band potential (E_{VB}) of $Bi_7O_9I_3$ and Fe-Bi/$Bi_7O_9I_3$/OVs were 2.36 and 2.22 eV (*vs.* NHE), respectively. Therefore, the energy band structures of $Bi_7O_9I_3$ and Fe-Bi/$Bi_7O_9I_3$/OVs were exhibited in Fig. 3f.

The removal of TC in HE-VL-PEF process over Fe-Bi/$Bi_7O_9I_3$/OVs and $Bi_7O_9I_3$ was further illustrated in Fig. 4a. Fe-Bi/$Bi_7O_9I_3$/OVs exhibited better removal efficiency (91.91%) in HE-VL-PEF process with the rate constants value of 0.035 min^{-1}, which was almost 2.2 times higher than $Bi_7O_9I_3$ (0.016 min^{-1}). And when the reaction time was extended to 2 h, the TC could be 100% removed (Fig. S7 in Supporting information). Furthermore, as shown in Fig. 4b, Fe-Bi/$Bi_7O_9I_3$/OVs also exhibited the higher H_2O_2 utilization efficiency (80.16%), which was about 1.77 times higher than $Bi_7O_9I_3$ (45.29%). The excellent catalytic degradation performance of Fe-Bi/$Bi_7O_9I_3$/OVs might be due to its efficient activation of H_2O_2 to produce more active species. Herein, the concentrations of ·OH produced in the HE-VL-PEF process over $Bi_7O_9I_3$ and Fe-Bi/$Bi_7O_9I_3$/OVs were further detected. As displayed in Fig. 4c, the $Bi_7O_9I_3$ in HE-VL-PEF process could generate only 59.16 μmol/L at 90 min, while that of Fe-Bi/$Bi_7O_9I_3$/OVs could reach to 244.48 μmol/L (4.13 times as much as $Bi_7O_9I_3$). This result indicated that H_2O_2 could be more efficiently activated and conversed into ·OH in HE-VL-PEF process with Fe-Bi/$Bi_7O_9I_3$/OVs. And the superior H_2O_2 activation performance of Fe-Bi/$Bi_7O_9I_3$/OVs might result from the Fe doping, which supplied active site and constructed Fenton reaction in the presence of H_2O_2. In the meantime, the formation of Bi and oxygen vacancy could effectively improve the separation efficiency of photogenerated carriers to further accelerate the transformation of Fe(III) to Fe(II), achieving Fenton reaction recycling. Notably, compared with $Bi_7O_9I_3$, a significant increased intensity of DMPO-·OH was observed with Fe-Bi/$Bi_7O_9I_3$/OVs as catalyst, which was consistent with the H_2O_2 utilization efficiency (HUE), the concentrations of ·OH produced and the performance of TC removal (Fig. 4d). Moreover, the EPR spectra of DMPO-·O_2^- with Fe-Bi/$Bi_7O_9I_3$/OVs as catalyst also appeared a significant increased intensity, just like the EPR spectra of DMPO-·OH (Fig. S8 in Supporting information).

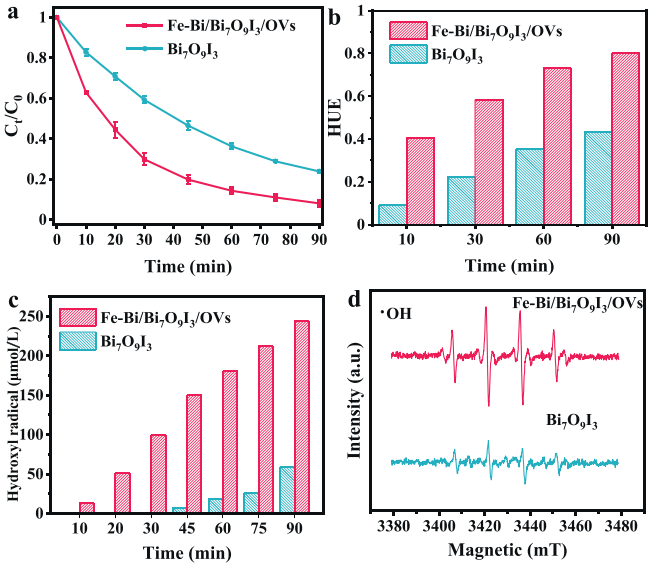

Fig. 4. (a) The removal performance of TC. (b) the H_2O_2 utilization efficiency. (c) The total concentrations of ·OH produced. (d) EPR spectra of DMPO-·OH in HE-VL-PEF process over Fe-Bi/$Bi_7O_9I_3$/OVs and $Bi_7O_9I_3$.

TC was removed in HE-VL-PEF process with multiple catalytic reactions (including photocatalysis, AO-H_2O_2, AO-VL-H_2O_2, and HE-EF). Hence, the comparison of different processes needs to be further investigated. As shown in Figs. 5a and b, compared with the photolysis process with visible light, Fe-Bi/$Bi_7O_9I_3$/OVs as catalyst in photocatalysis process could remove 22.47% of TC with the re-

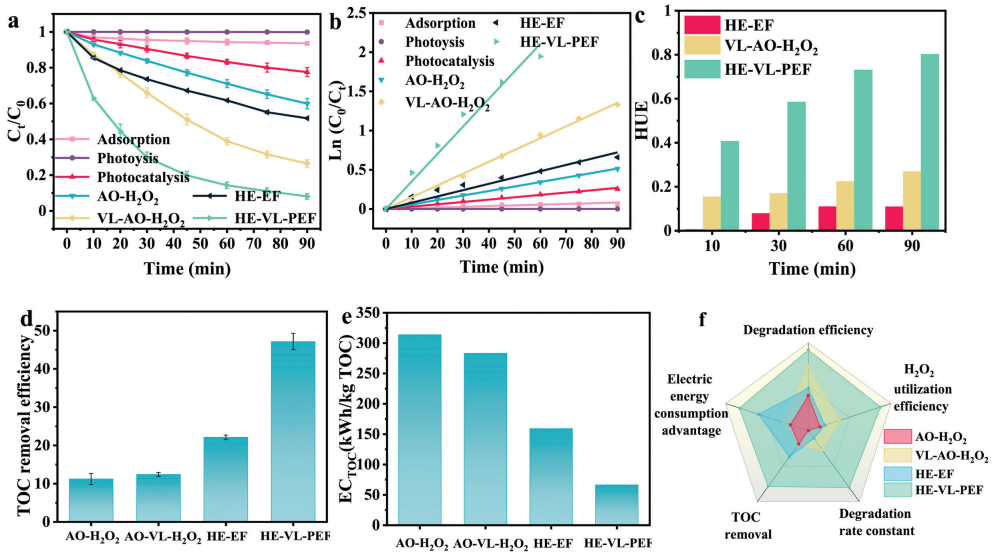

Fig. 5. (a)TC degradation in different process. (b) The corresponding *k* values. (c) The H_2O_2 utilization efficiency, (d) TOC removal, (e) electric energy consumption of different process. (f) Radar chart of the performances for HE-VL-PEF process.

action rate constant of 0.003 min^{-1} in 90 min, which indicated Fe-Bi/$Bi_7O_9I_3$/OVs was an effective visible light photocatalyst. For AO-H_2O_2 process, only 40.09% of TC could be removed, and the accumulation concentration of H_2O_2 could reach to 89.35 mg/L, which attributed to efficient H_2O_2 electrosynthesis performance of NADE (Fig. 5a and Fig. S9 in Supporting information). Moreover, the combination of AO-H_2O_2 and LED visible light (VL-AO-H_2O_2) showed a better TC removal (73.57%) than that of AO-H_2O_2 (Fig. 5a), but unfortunately its total organic carbon (TOC) removal rate was still similar to AO-H_2O_2, indicating the H_2O_2 could be activated and decomposed under LED visible light illumination with limited ROS generation. For HE-EF process, approximately 48.27% TC could be removed after 90 min. However, the HUE of Fe-Bi/$Bi_7O_9I_3$/OVs in HE-EF process was not ideal, only 10.90% in 90 min (Fig. S9 and Fig. 5c). In order to improve H_2O_2 utilization efficiency, TC removal efficiency and mineralization efficiency, we introduced LED visible light into HE-EF process to construct HE-VL-PEF process. Surprisingly, HE-VL-PEF process could achieve 91.91% removal of TC (0.035 min^{-1}), 47.16% removal of TOC and 80.16% of HUE (Figs. 5a-d), demonstrating the remarkably enhanced catalytic performance of Fe-Bi/$Bi_7O_9I_3$/OVs under the existence of H_2O_2 and visible light irradiation.

The removal of TOC in different processes was further illustrated in Fig. 5d. Obviously, HE-VL-PEF process exhibited the higher removal efficiency of TOC (47.16%) than that of HE-EF (22.11%), VL-AO-H_2O_2 (12.43%) and AO-H_2O_2 (11.21%). The major intermediate products were identified by HPLC/MS analysis. Based on the mass/charge ratios (*m/z*) of the detected species (Table S1 in Supporting information), the possible degradation pathway of TC in HE-VL-PEF was proposed in Fig. S10 (Supporting information). Meanwhile, further calculation in Fig. 5e demonstrated the electric energy consumption (EEC) of HE-VL-PEF was 66.34 kWh/kg TOC, which was only 21.13% of that in AO-H_2O_2 (313.89 kWh/kg TOC), 23.42% of that in VL-AO-H_2O_2 (283.19 kWh/kg TOC) and 41.67% of that in HE-EF (159.18 kWh/kg TOC), indicating HE-VL-PEF process was more cost-effective for the treatment of organic wastewater. The results showed that the introduction of Fe-Bi/$Bi_7O_9I_3$/OVs and visible light promoted the mineralization of pollutant and reduced EEC. The above results clearly demonstrate that HE-VL-PEF process presented performance superiorities in pollutant removal, mineralization, HUE, and EEC (Fig. 5f). Moreover, compared with other related works (PF, EF and PEF process), HE-VL-PEF process with Fe-Bi/$Bi_7O_9I_3$/OVs as catalyst (LED visible light irradiation) and NADE as cathode (without aeration) performed lower electric energy consumption and better cyclic degradation performance (Table S2 in Supporting information), which demonstrated once again that it was a high-efficiency, low-consumption and promising technology for wastewater treatment.

To optimize the operational conditions for the degradation of TC in HE-VL-PEF process, the effects of the applied current, catalyst dosage, and initial pH on the TC degradation were investigated in Fig S11. The background constituents in aqueous matrix are usually complex, thus the influence of inorganic anions (Cl^-, NO_3^-, HPO_4^{2-}, and HCO_3^-) and humic acid (HA) on TC removal in HE-VL-PEF process was investigated in Fig S12 (Support information).

To investigate the contribution of major active species responsible for TC degradation in HE-VL-PEF process, free radical quenching experiments were carried out. The triethanolamine (TEOA), methanol (MeOH) and SOD (Superoxide Dismutase) were chosen for scavenging photogenerated holes (h^+), $^{\bullet}OH$, and superoxide radical ($^{\bullet}O_2^-$), respectively. As shown in Fig. 6a, the degradation efficiency of TC decreased mildly to 82.21% by addition of SOD, manifesting that the contributions of $^{\bullet}O_2^-$ on TC removal was weak. It was obvious that when MeOH and TEOA were added to the reaction system, the TC degradation efficiency declined by 28.14% and 17.75% along with the corresponding reaction rate constant from 0.035 to 0.012 and 0.016 min^{-1} (Figs. 6a and b), respectively, indicating that $^{\bullet}OH$ and h^+ were the predominant reactive species and $^{\bullet}OH$ played the leading role. In order to clearly verify the contribution of different active species, the contribution rate was further calculated according to Eq. S3 (Supporting information). As shown in Fig. 6b, the relative contributions of $^{\bullet}OH$, h^+ and $^{\bullet}O_2^-$ to the overall degradation kinetics were determined to be 64.22%, 52.89%, and 38.64%, respectively. Notably, the total contribution exceeds 100% due to the convoluted radical chemistry involved in photocatalysis [39-41]. In short, $^{\bullet}OH$, h^+ and $^{\bullet}O_2^-$ all conducted to the TC removal, while $^{\bullet}OH$ played a dominant role in HE-VL-PEF process.

The EPR experiments were further conducted to clarify the formation of $^{\bullet}OH$ and $^{\bullet}O_2^-$ in different processes. As displayed in Figs. 6c and d, compared with AO-H_2O_2, AO-VL-H_2O_2, and HE-EF process, HE-VL-PEF process exhibited the strongest intensity of DMPO-$^{\bullet}OH$ signals and the DMPO-$^{\bullet}O_2^-$ signals, indicating that Fe-Bi/$Bi_7O_9I_3$/OVs and visible light could promote the H_2O_2 activa-

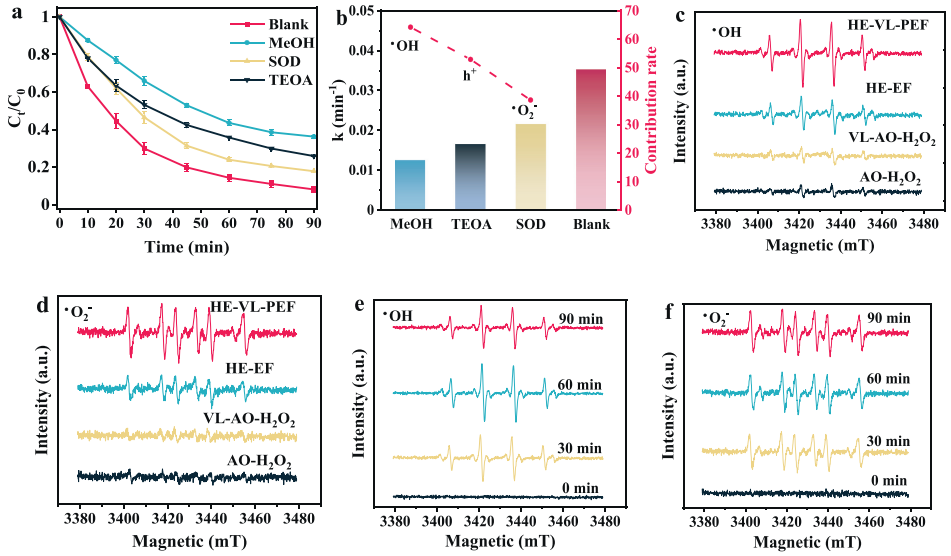

Fig. 6. (a) The quenching experiments for TC degradation with different radical scavengers in HE-VL-PEF process. (b) The reaction kinetic constants and free radical contribution of TC degradation in HE-VL-PEF process. (c) EPR spectra of DMPO-·OH and (d) DMPO-$·O_2^-$ adduct in different process. (e) EPR spectra of DMPO-·OH and (f) DMPO-$·O_2^-$ adduct at different reaction during HE-VL-PEF process with Fe-Bi/$Bi_7O_9I_3$/OVs.

tion to generate more ROS and improve TC degradation efficiency. We also further compared the generated ·OH concentration in HE-VL-PEF process with that of HE-EF process. The ·OH concentration in HE-VL-PEF process (244.48 μmol/L) was much higher that of HE-EF process (3.51 μmol/L) (Fig. S13 in Supporting information). In order to further confirm the transformation of ≡Fe(III) to ≡Fe(II) by photoelectrons during HE-VL-PEF, we investigated the changes of ≡Fe(II) ratio before and after the reaction. As shown in Fig. S14a (Supporting information), there was no significant change in ≡Fe(II) ratio after HE-EF process (from 0.36 to 0.35). However, the ≡Fe(II) ratio increased from 0.36 to 0.58 after HE-VL-PEF process (Fig. S14b in Supporting information). Thus, it could be reasonably concluded that HE-VL-PEF process with Fe-Bi/$Bi_7O_9I_3$/OVs achieved photoelectrons to accelerate the transformation of Fe(III) to Fe(II) and directly activate H_2O_2 for the continuous production of active species. Moreover, the EPR spectra of DMPO-·OH and DMPO-$·O_2^-$ adduct maintained high intensity at different reaction time during HE-VL-PEF process with Fe-Bi/$Bi_7O_9I_3$/OVs (Figs. 6e and f), which indicated the continuous production of ·OH and $·O_2^-$.

To further reveal the influence of Fe-doping on the excitation and transfer of electrons, the density of states (DOS) of Fe-Bi/$Bi_7O_9I_3$/OVs and $Bi_7O_9I_3$ were calculated using a hybrid DFT method. After Fe-doping, intermediate levels can be observed in the forbidden band of Fe-Bi/$Bi_7O_9I_3$/OVs comparing with $Bi_7O_9I_3$ (Fig. 7a). In this case, photogenerated e^- can be easily excited and transferred from VB to intermediate levels, which will be more favorable to inhibit the recombination of photogenerated e^--h^+ pairs. Furthermore, the DOS exhibits that the band gap of Fe-Bi/$Bi_7O_9I_3$/OVs is narrower than that of the $Bi_7O_9I_3$, which is consistent with the conclusion obtained by analyzing the band structure (Figs. 7a and 3f).

Bader charge analysis and charge density difference reveal that the e^- loss capacity of Fe site in Fe-Bi/$Bi_7O_9I_3$/OVs is stronger than that of Bi site in $Bi_7O_9I_3$ (Fig. 7b and Table S3 in Supporting information). This result indicates that Fe as the active site can acquire more electrons in Fe-Bi/$Bi_7O_9I_3$/OVs, achieving the transformation of Fe(III) to Fe(II). Furthermore, the electronic location function (ELF) exhibits that there is a stronger covalent interaction on the surface of Fe-Bi/$Bi_7O_9I_3$/OVs compared with $Bi_7O_9I_3$ (Fig. 7c and Fig. S15 in Supporting information), and a faster electron transport channel is formed between O-Fe.

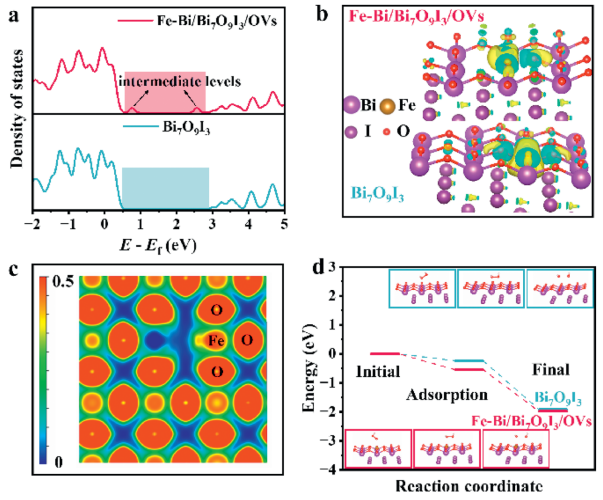

Fig. 7. (a) Calculated DOS and (b) Charge density difference of Fe-Bi/$Bi_7O_9I_3$/OVs and $Bi_7O_9I_3$. (c) Electronic location function (ELF) of Fe-Bi/$Bi_7O_9I_3$/OVs. (d) Calculated free energy of H_2O_2 activation to ·OH on (inset with the corresponding intermediate structures).

To further explore the activation mechanism of H_2O_2 during the HE-VL-PEF process of Fe-Bi/$Bi_7O_9I_3$/OVs, the Gibbs free energy of the reaction was calculated in Fig. 7d. The adsorption process is an important reaction step for H_2O_2 activation, and the more negative adsorption energy on the Fe-Bi/$Bi_7O_9I_3$/OVs manifests that the H_2O_2 adsorption efficiency on it is higher. And the corresponding transition energies for activating H_2O_2 into *OH were −1.91 eV ($Bi_7O_9I_3$) and −1.98 eV (Fe-Bi/$Bi_7O_9I_3$/OVs), respectively. Hence, Fe-O-Bi is more prone to O-O fracture (the key rate-limiting step of H_2O_2 activation), facilitating the formation of *OH. In conclusion, the introduction of Fe as the active site is more beneficial to activate H_2O_2 and generate more ·OH.

Hence, the possible mechanism of TC degradation in HE-VL-PEF process was elucidated in Fig. 8. First of all, NADE electrogenerated sufficient H_2O_2 without aeration. Under visible light irradiation, the photogenerated electrons on the VB of Fe-Bi/$Bi_7O_9I_3$/OVs were excited to the intermediate defect level formed by the oxy-

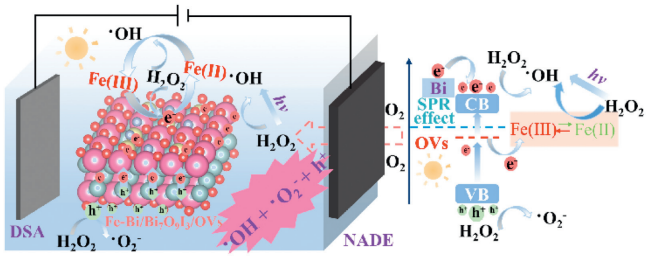

Fig. 8. The possible mechanism of TC degradation in HE-VL-PEF process with Fe-Bi/$Bi_7O_9I_3$/OVs as catalyst and NADE as cathode.

gen vacancies, then a part of the photogenerated electrons at the defect level could be excited to the CB for directly activating H_2O_2 to generate ·OH (Eqs. 2 and 3), and another part of photogenerated electrons would transfer to the Fe-doped site on the surface of catalyst to reduce ≡Fe(III) to ≡Fe(II) (Eq. 4), overcoming the rate-limiting step of the EF (Eq. 5). Subsequently, the ≡Fe(II) sites could efficiently activate H_2O_2 to generate ·OH for enhanced pollutant removal and mineralization (Eq. 6), while themselves were oxidized to ≡Fe(III) (Eq. 6), achieving effective cyclic conversions of ≡Fe(III)/≡Fe(II). Notably, because of SPR effect of enhancing surface electron excitation and interfacial electron transfer, the photoinduced electrons generated from Bi also would transfer to the CB of Fe-Bi/$Bi_7O_9I_3$/OVs for directly activating H_2O_2 (Eq. 3) [42]. The photogenerated h^+ left in VB of Fe-Bi/$Bi_7O_9I_3$/OVs could react with H_2O_2 forming $^{\bullet}O_2^-$ for degradation or directly oxidize TC (Eq. 7) [43,44]. Moreover, the ·OH was also produced by direct photolysis of H_2O_2 (Eq. 8) [45]. Eventually, with the cooperation of generated active radicals, TC could be efficiently degraded and further mineralized into CO_2 and H_2O (Eq. 9).

$$\text{Fe} - \text{Bi/Bi}_7\text{O}_9\text{I}_3\text{/OVs} + h\nu \rightarrow h^+ + e^- \quad (2)$$

$$e^- + H_2O_2 \rightarrow {}^{\bullet}OH + OH^- \quad (3)$$

$$\equiv Fe(III) + e^- \rightarrow \equiv Fe(II) \quad (4)$$

$$\equiv Fe(III) + H_2O_2 \rightarrow \equiv Fe(II) + {}^{\bullet}O_2H + H^+ \quad (5)$$

$$\equiv Fe(II) + H_2O_2 \rightarrow \equiv Fe(III) + {}^{\bullet}OH + OH^- \quad (6)$$

$$h^+ + H_2O_2 \rightarrow {}^{\bullet}O_2^- \quad (7)$$

$$h\nu + H_2O_2 \rightarrow 2{}^{\bullet}OH \quad (8)$$

$$h^+ + {}^{\bullet}OH + {}^{\bullet}O_2^- + TC \rightarrow CO_2 + H_2O + \text{small molecules} \quad (9)$$

To evaluate the stability and the reusability of Fe-Bi/$Bi_7O_9I_3$/OVs, cyclic TC degradation experiments were conducted. The catalyst was collected by vacuum filtration after reaction, rinsed with ultrapure water and then dried in an oven at 60 °C overnight to conduct next photocatalytic cycle. The degradation efficiency of TC decreased by only 1.49% after ten cycles and all reached more than 90% (Fig. 9a). In addition, the iron leaching concentration of Fe-Bi/$Bi_7O_9I_3$/OVs was significantly lower than the European Union environmental standard (2 mg/L) during 10 cycles of degradation (Fig. 9b) [46]. The XRD and XPS spectra were utilized to further evaluate the stability of catalyst. As shown in Figs. 9c and d, the XRD and XPS spectra of Fe-Bi/$Bi_7O_9I_3$ after ten cycles was almost identical to that of fresh catalyst except for a slight decrease in peak intensity, manifesting that it kept

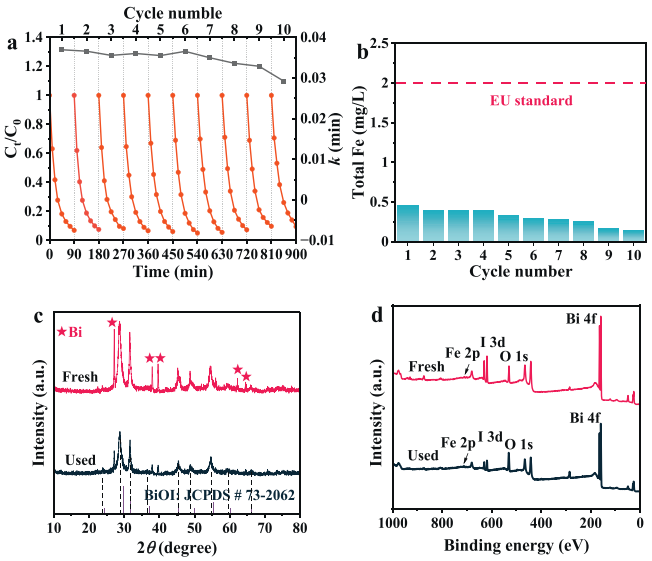

Fig. 9. (a) Cycling experiments of TC in Fe-Bi/$Bi_7O_9I_3$/HE-VL-PEF process. (b) Fe leaching after each cycle. (c) XRD patterns and (d) XPS spectra of Fe-Bi/$Bi_7O_9I_3$ before and after cycles.

its intrinsically crystal structure during HE-VL-PEF degradation of TC. The SEM and TEM images of Fe-Bi/$Bi_7O_9I_3$/OVs after cycling tests proved that it kept the hierarchical flower-like microspheres architecture (Fig. S16 in Supporting information).

In summary, a novel three-dimensional flower-like Fe-Bi/$Bi_7O_9I_3$/OVs was prepared, and further coupled with NADE to construct the HE-VL-PEF process, which significantly promoted the degradation and mineralization of TC. The synergistic effect of OVs and Bi with SPR effect significantly improves the photocatalytic performance of Fe-Bi/$Bi_7O_9I_3$/OVs under visible light irradiation. The existence of Bi broadens the light response range of Fe-Bi/$Bi_7O_9I_3$/OVs. Meanwhile, the generated OVs can improve the separation efficiency of photogenerated carriers to further accelerate the transformation of Fe(III) to Fe(II), achieving Fenton reaction recycling. Additionally, the HE-VL-PEF process with Fe-Bi/$Bi_7O_9I_3$/OVs as catalyst and NADE as cathode combined the advantages of EF and PF, achieving excellent H_2O_2 *in-situ* electrosynthesis performance (no aeration) and activation performance (visible light). As expected, HE-VL-PEF process presented more excellent pollutant removal (91.91%) and lower electric energy consumption (66.34 kWh/kg TOC). These results indicated that Fe-Bi/$Bi_7O_9I_3$/OVs was a promising catalyst and gained a promising insight towards EF coupled with PF for high-efficiency and low-consumption degradation of pollutant.

Declaration of competing interest

The authors declare that they have no known competing financial interests or personal relationships that could have appeared to influence the work reported in this paper.

CRediT authorship contribution statement

Ruiheng Liang: Formal analysis, Investigation, Methodology, Writing – original draft. **Huizhong Wu:** Data curation, Investigation, Methodology, Validation. **Zhongzheng Hu:** Data curation, Investigation, Methodology. **Ge Song:** Data curation, Validation. **Xuyang Zhang:** Data curation, Validation. **Omotayo A. Arotiba:** Validation. **Minghua Zhou:** Conceptualization, Funding acquisition, Methodology, Supervision, Writing – review & editing.

Acknowledgments

This work was financially supported by Key Project of Natural Science Foundation of Tianjin (No. 21JCZDJC00320), National Key R&D Program International Cooperation Project (No. 2021YFE0106500), Natural Science Foundation of China (No. 52170085), Fundamental Research Funds for the Central Universities, Nankai University, and National Research Foundation IRG-China/South Africa Research Cooperation Programme (No. 132793).

Supplementary materials

Supplementary material associated with this article can be found, in the online version, at doi:10.1016/j.cclet.2024.110136.

References

[1] X. Zhang, B. Xu, S. Wang, et al., Appl. Catal. B: Environ. 306 (2022) 121119.
[2] Z. Zhang, J. Liang, W. Zhang, et al., Appl. Catal. B: Environ. 330 (2023) 122621.
[3] P. Kovalakova, L. Cizmas, T.J. McDonald, et al., Chemosphere 251 (2020) 126351.
[4] L. Xu, H. Zhang, P. Xiong, et al., Sci. Total Environ. 753 (2021) 141975.
[5] S. Park, S. Kim, Y. Yea, et al., J. Hazard. Mater. 443 (2023) 130165.
[6] Z. Liu, Z. Gao, Q. Wu, et al., Chem. Eng. J. 423 (2021) 130283.
[7] N. Amaly, A.Y. El-Moghazy, N. Nitin, G. Sun, P.K. Pandey, Chem. Eng. J. 430 (2022) 133077.
[8] M.R. Haider, W.L. Jiang, J.L. Han, et al., Environ. Sci. Technol. 57 (2023) 18668–18679.
[9] X. Zhang, X. Wang, X. Zhang, et al., Electrochim. Acta 472 (2023) 143437.
[10] X. Qin, P. Cao, X. Quan, et al., Environ. Sci. Technol. 57 (2023) 2907–2917.
[11] Z. Wang, Y. Du, P. Zhou, et al., Chem. Eng. J. 454 (2023) 140096.
[12] G. Song, X. Du, Y. Zheng, et al., J. Hazard. Mater. 422 (2022) 126888.
[13] F. Deng, H. Olvera-Vargas, M. Zhou, et al., Chem. Rev. 123 (2023) 4635–4662.
[14] X. Wang, J. Jing, M. Zhou, R. Dewil, Chin. Chem. Lett. 34 (2023) 107621.
[15] Y. Lin, P. Huo, F. Li, et al., Chem. Eng. J. 450 (2022) 137948.
[16] J.J. Conde, S. Abelleira, S. Estévez, et al., J. Environ. Manage. 332 (2023) 117308.
[17] L.G. Devi, B.G. Anitha, Surf. Interfaces 11 (2018) 48–56.
[18] X. Bai, Y. Li, L. Xie, et al., Environ. Sci. Nano 6 (2019) 2850–2862.
[19] T. Jia, J. Wu, Z. Ji, et al., Appl. Catal. B: Environ. 284 (2021) 119727.
[20] W. An, H. Wang, T. Yang, et al., Chem. Eng. J. 451 (2023) 138653.
[21] Z. Wu, J. Shen, W. Li, et al., Appl. Catal. B: Environ. 330 (2023) 122642.
[22] X.A. Dong, W. Zhang, Y. Sun, et al., J. Catal. 357 (2018) 41–50.
[23] Z.J. Liu, J.Q. Wan, Z.C. Yan, Y. Wang, Y.W. Ma, Chem. Eng. J. 433 (2022) 133767.
[24] Y. Su, Q. Zhang, G. Song, et al., Sep. Purif. Technol. 301 (2022) 122038.
[25] Q. Zhang, M. Zhou, G. Ren, et al., Nat. Commun. 11 (2020) 1731.
[26] R. Ma, S. Zhang, X. Liu, et al., Chemosphere 286 (2022) 131783.
[27] X. Geng, W. Li, F. Xiao, et al., Catal. Sci. Technol. 7 (2017) 658–667.
[28] C. Zhu, Y. Wang, L. Qiu, et al., Sep. Purif. Technol. 290 (2022) 120878.
[29] Y. Bai, H. Bai, K. Qu, et al., Chem. Eng. J. 362 (2019) 349–356.
[30] T. Zhang, Z. Li, J. Zhong, J. Li, X. Tang, Surf. Interfaces 31 (2022) 102051.
[31] Y. Zhao, Y. Zhao, R. Shi, et al., Adv. Mater. 31 (2019) 1806482.
[32] Q. Zhu, R. Hailili, Y. Xin, et al., Appl. Catal. B: Environ. 319 (2022) 121888.
[33] Z. Liu, L. Wang, X. Yu, et al., Adv. Funct. Mater. 29 (2019) 1807279.
[34] Y. Sun, Z. Zhao, W. Zhang, et al., J. Colloid Interf. Sci. 485 (2017) 1–10.
[35] C. Yue, L. Zhu, Y. Qiu, et al., J. Clean. Prod. 392 (2023) 136017.
[36] X. Liu, H. Zhou, S. Pei, S. Xie, S. You, Chem. Eng. J. 381 (2020) 122740.
[37] L. Ye, D. Wang, S. Chen, ACS Appl. Mater. Interfaces 8 (2016) 5280–5289.
[38] A. Kumar, G. Sharma, A. Kumari, et al., Appl. Catal. B: Environ. 284 (2021) 119808.
[39] Y. Wu, J. Chen, H. Che, et al., Appl. Catal. B: Environ. 307 (2022) 121185.
[40] W. Wang, Q. Niu, G. Zeng, et al., Appl. Catal. B: Environ. 273 (2020) 119051.
[41] P. Chen, L. Blaney, G. Cagnetta, et al., Environ. Sci. Technol. 53 (2019) 1564–1575.
[42] J. Ding, C. Li, H. Yin, et al., Environ. Pollut. 327 (2023) 121550.
[43] G. Jiang, X. Wang, B. Zhu, et al., Carbon 190 (2022) 32–46.
[44] R. Liang, Z. Hu, H. Wu, et al., Sep. Purif. Technol. 314 (2023) 123591.
[45] S. Xin, S. Huo, C. Zhang, et al., Appl. Catal. B: Environ. 305 (2022) 121024.
[46] C. Zhao, L. Meng, H. Chu, et al., Appl. Catal. B: Environ. 321 (2023) 122034.